IEEE *Access*

Multidisciplinary : Rapid Review : Open Access Journal

Dynamics and Model Predictive Control of Current-Fed Dickson Voltage Multiplier: TS Fuzzy Approach

YOUSEF NIAZI[1], AMIRHOSSEIN RAJAEI [1], (Member, IEEE), MOHSEN FARBOOD[1],
VAHID MORADZADEH TEHRANI[1], MOKHTAR SHASADEGHI[1],
AND MAHDI SHAHPARASTI [2], (Senior Member, IEEE)
[1]Department of Electrical and Electronics Engineering, Shiraz University of Technology, Shiraz 71557-13876, Iran
[2]School of Technology and Innovations, Flexible Energy Resources, University of Vaasa, 65200 Vaasa, Finland

Corresponding author: Mahdi Shahparasti (mahdi.shahparasti@uwasa.fi)

ABSTRACT This study presents a new approach to modeling and control the current-fed Dickson voltage multiplier (CF-DVM). The capacitor voltage relation and the input current are obtained. As all switching intervals are considered in detail, a highly accurate dynamic model is obtained, which can be easily extended for a CF-DVM with an arbitrary number of stages. Using the precise extracted model, the Takagi-Sugeno fuzzy model (TSFM) of the CF-DVM is provided, which is an exact equivalent representation of the CF-DVM nonlinear model. Then, a highly accurate and responsive model predictive controller (MPC) is designed based on an obtained TSFM of the CF-DVM to control the output voltage in an optimal and constrained manner. To obtain the control signal, the suggested optimization problem is converted to a quadratic programming (QP)-based problem which has a low online computational burden. Moreover, the performance of the proposed MPC is compared with the PI controller and the linear MPC. Finally, the simulation and experimental results demonstrate the promising merits of the proposed model and control approaches.

INDEX TERMS DC-DC boost converter, current-fed Dickson voltage multiplier, TS fuzzy model, model predictive control.

I. INTRODUCTION
Utilizing small-size renewable resources have been rapidly increased in recent years. One of the most significant applications of the power electronic (PE) converters is integrating the power generation of the micro-sources [1]. Because the output voltage of renewable resources is generally low, high step-up DC/DC converters are required to boost the output voltage [2]. These converters can be categorized as isolated and non-isolated converters [3].

The voltage gain can be adjusted by changing the winding turn ratio in the isolated structures. However, achieving a very high voltage gain requires a high turn ratio, which increases the converter's weight, volume, cost [3] and often necessitates employing snubber circuits due to the high voltage spikes

The associate editor coordinating the review of this manuscript and approving it for publication was Chi-Seng Lam.

across the semiconductors caused by the leakage inductance [4]. Compared to the isolated converters, non-isolated DC/DC converters offer simplicity, compact size, and low cost [3]. However, the classical non-isolated boost converters are unable to achieve a high voltage gain at extremely-high duty cycles (*D*) due to excessive conduction losses [3], minimal efficiency [4], poor transient response [2], and protection issues.

To address these limitations, different techniques and structures were proposed in the literature [2], such as switched-inductor (SI) [5], switched-capacitor (SC) cells, switched-capacitor-inductor (SCI) networks [3], coupled inductors [6], and non-coupled inductors [7], including the cascaded converters and voltage multipliers (VM) [8].

The SC-based converters are inductor-less circuits that step up/down the input voltage [9]. The absence of magnetic elements in these converters leads to a high-power

density [10], [11]. However, their output voltage regulation is limited due to the discrete nature of stages and voltage gain. Moreover, the capacitor charging and discharging rapidly in voltage-fed (VF) structures generates input inrush current [12]. In response to these issues, an inductor or current source can be integrated into the SC converters, also leading to soft switching of semiconductor switches and enhanced efficiency [1], [2], [13]. The SC converters applications include high side MOSFET gate drive circuitry [2], battery charge stabilization [14], high-efficiency DC/DC converters [11], photovoltaic (PV) interface systems [15], power supply processors, flash memory [13], fuel cell (FC) [16], energy extraction [17], and IoT systems [18].

The most well-known SC-VMs are Cockcroft-Walton (CWVM), Fibonacci (FVM), and Dickson (DVM) voltage multipliers. Compared to other structures, the DVM can provide a high voltage gain with a low output impedance anis independent of parasitic capacitors, particularly for many stages [19]. Thus, the DVM is appropriate for high step-up applications [2]. Nevertheless, to achieve a high voltage gain with SC converters, some limitations should be considered, such as input peak current, the effect of charging and discharging capacitors, voltage level, number of stages, the impact of the parasitic elements on the circuit's performance [20]–[22].

The DVM switching is accomplished by pulse-width-modulation (PWM); hence, throughout employing a control system, the output voltage can be regulated around an operating point even during input voltage and output load disturbances. The controller design process requires mathematical equations and analysis of the converter. A dynamic model of the DVM was derived in [23], [24]. However, one operation mode is ignored for simplicity, reducing the derived model's accuracy. Furthermore, a bilinear model for controller design is extracted in [25]. However, the model contains only two operating modes, while CS converters have several operating modes. Another dynamic model is represented in [26], with a phase-shift switching strategy, where time intervals are identified. However, for the non-phase-shift method, other time intervals must be calculated.

Other studies also considered the output voltage regulation [27]–[29]. A sliding mode controller (SMC) was implemented based on the linearized model of the SC converter in [27]. Also, a dynamic modeling and controller design for a high step-up DC/DC converter is provided in [28] using a reduced-order model. Then, the control design is provided based on the linear systems theorem by obtaining the linear model of the converter.

Model predictive control (MPC) is a very effective control method that has been employed to regulate the output voltage of the converters [30], [31]. In the MPC strategy, a dynamic model of the system is used to predict the system's future behavior [32]. The control signal is calculated based on an optimization problem. The accuracy of the adopted model in the MPC scheme directly affects the controller's performance. In [30], a linear model and MPC method were
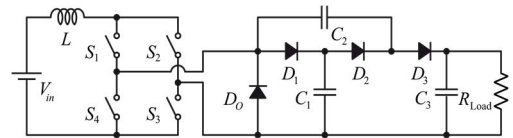

FIGURE 1. Current-fed DVM [16].

proposed to control a constant switching frequency DC/DC converter. Also, a maximum power point tracking (MPPT) approach was designed for PV systems based on the given MPC. In [29], a fuzzy-based MPC was proposed based on the linear matrix inequality (LMI) to regulate the output voltage of a DC/DC boost converter. To do this, the Takagi-Sugeno fuzzy model (TSFM) of the converter was obtained, and the control signal was calculated based on the LMI-based online optimization problem. However, the proposed LMI-based optimization problem is computational heavy. A computationally efficient MPC for a DC/DC boost converter was designed in [33], based on the linear model and continuous time.

This study proposes a highly accurate dynamic model by considering all operating intervals with no simplification compared to [23], [34], and also an MPC controller design based on an obtained TSFM for a two-stage CF-DVM to regulate the output voltage. The proposed method can easily be extended for any desired stages. The fuzzy-based MPC is designed based on the quadratic optimization problem. Additionally, the proposed TSFM is presented based on the sector nonlinearity approach, which represents an exact approximation of the nonlinear dynamic model of the CF-DVM. Then, the optimization problem of the nonlinear MPC is converted to quadratic programming (QP)-based MPC compared to [29], [35], which has the benefit of a very low online computational burden compared to [36]. Finally, the advantages of the proposed approach compared with existing studies are as follows:

Dynamic modeling: Compared to [23], [24] 1) the dynamic equations are derived based on accurate calculation of time intervals of each operation mode and 2) there is no simplification or/and integration in the modes of operations.

Controller method: Compared to [29], [35], [36] 1) the nonlinear MPC process converted to solving an QP optimization problem and 2) the online computational burden is greatly reduced.

This paper is organized as follows: In section II, the dynamic modeling of the CF-DVM is presented. In section III, the fuzzy-based MPC of the CF-DVM is designed. Then, simulations and experiments in section IV validate the accuracy and merits of the proposed model and control approach. Finally, the paper is concluded in section V.

II. DYNAMIC MODELING OF THE CF-DVM
In this section, the converter topology and operating states are explained. Then the dynamic model of the CF-DVM is extracted using the state-space averaging method.
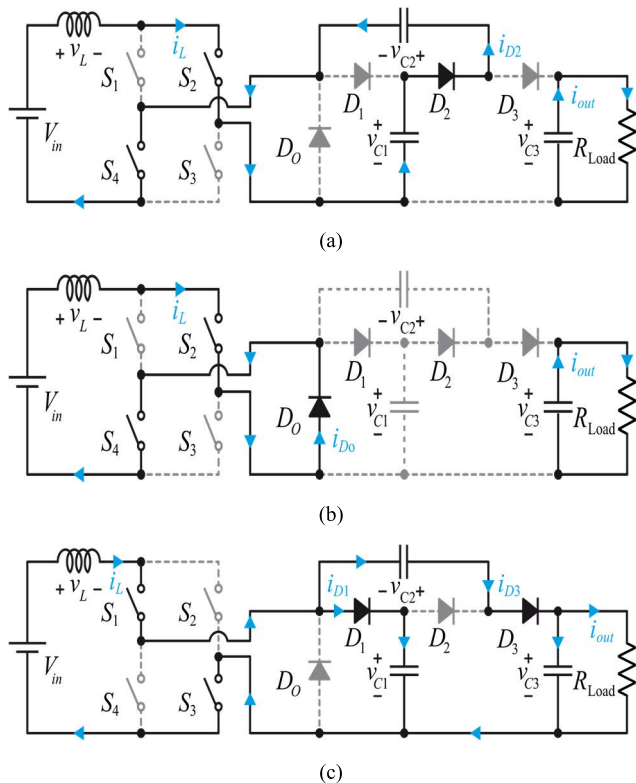
FIGURE 2. Circuit configuration and current paths for different operation modes: a) [$d1T$], b) [$(D-d1)T$], c) [$(1-D)T$].

A. EXTRACTING LARGE-SIGNAL MODEL OF THE CF-DVM

The structure of the two-stage CF-DVM is shown in Figure 1. The CCM operation includes three operating modes, as discussed in the following. Equivalent circuits with the current flow path in each state and the main waveforms with associated timing are illustrated in Figure 2 and Figure 3, respectively. It is hypothesized that the converter operates in steady-state CCM, S_1-S_4 have no deadtime, and all components are ideal except for the diodes with an internal resistor r_d.

*Mode*1 ($d1T$): In the time interval of $d1T$, S_2 and S_4 are conducting. The inductor current (i_l) passes through $C_1 - D_2 - C_2$ current flow path as shown in Figure 2(a). As a result, the voltage across the capacitor C_1 (v_{c1}) decreases, and the voltage across the capacitor C_2 (v_{c2}) increases. This condition lasts until the voltages of the capacitors C_1 and C_2 become equal. Furthermore, the capacitor C_3 supplies the load current and gets discharged. The state equations are given by:

$$\begin{cases} L\dfrac{di_L}{dt} = v_{in} + v_{C1} - v_{C2} - i_L r_d \\ C\dfrac{dv_{C1}}{dt} = -i_L \\ C\dfrac{dv_{C2}}{dt} = i_L \\ C\dfrac{dv_{C3}}{dt} = -\dfrac{v_{C3}}{R} \end{cases} \quad (1)$$

Mode 2 ($(D - d1)T$): In this mode, all switches maintain their previous state, i_L keeps its current flow path through diode D_0 and increases linearly by the input voltage source

(V_{in}). Diodes D_1, D_2, D_3 are reversed-biased. Therefore, there is no current flowing through capacitors C_1 and C_2. Capacitor C_3 discharge current supplies the load. The equivalent circuit of this state is shown in Figure 2(b). The relevant equations in this interval are given by:

$$\begin{cases} L\dfrac{di_L}{dt} = v_{in} - i_L r_d \\ C\dfrac{dv_{C1}}{dt} = 0 \\ C\dfrac{dv_{C2}}{dt} = 0 \\ C\dfrac{dv_{C3}}{dt} = -\dfrac{v_{C3}}{R} \end{cases} \quad (2)$$

Mode 3 ($(1 - D)T$): In this mode, S_2 and S_4 are OFF, and S_1 and S_3 are ON. The diodes D_1 and D_3 are forward-biased, while the other diodes are reversed-biased. Inductor current (i_L) flows through two current paths of $D_1 - C_1$ and $C_2 - D_3 - C_3$ in parallel. Consequently, i_L decreases. Capacitor C_2 is discharged, while capacitors C_1 and C_3 are charged. The equivalent circuit for this interval is shown in Figure 2(c). We use the diode current equations to obtain the inductor's voltage and the capacitors' current equations. For this purpose, diode current equations are extracted:

$$i_{D1} = \frac{1}{2r_d}(v_{C3} - v_{C2} - v_{C1}) + \frac{i_L}{2}, \quad (3)$$

$$i_{D3} = -\frac{1}{2r_d}(v_{C3} - v_{C2} - v_{C1}) + \frac{i_L}{2}, \quad (4)$$

$$\begin{cases} L\dfrac{di_L}{dt} = v_{in} - i_{D1}r_d - v_{C1} \\ C\dfrac{dv_{C1}}{dt} = i_{D1} = \dfrac{1}{2r_d}(v_{C3} - v_{C2} - v_{C1}) + \dfrac{i_L}{2} \\ C\dfrac{dv_{C2}}{dt} = -i_{D3} = \dfrac{1}{2r_d}(v_{C3} - v_{C2} - v_{C1}) - \dfrac{i_L}{2} \\ C\dfrac{dv_{C3}}{dt} = i_{D3} - \dfrac{v_{C3}}{R} = \dfrac{i_L}{2} - \dfrac{v_{C3}}{R} \\ \qquad - \dfrac{1}{2r_d}(v_{C3} - v_{C2} - v_{C1}) \end{cases} \quad (5)$$

The averaged state-space model of the converter can be obtained by applying the averaging state-space technique to (1), (2), and (5) as follows: (6)–(10), shown at the bottom of the next page, where the state space variables are:

$$\begin{bmatrix} i_L & v_{C1} & v_{C2} & v_{C3} \end{bmatrix}^T. \quad (11)$$

The parameter $d1$ can also be obtained in terms of D, where D is the duty cycle of S_2 and S_4. In the time interval of $d1T$, the charged energy Q_{C1} stored in C_1 is divided equally between C_1 and C_2. During the interval of $(1 - D)T$, capacitor C_1 receives the $Q_{C1}/2$ from the input source (V_{in}) through D_1. Capacitor C_2 also transfers the $Q_{C1}/2$ energy received from the previous step to the output load. As both capacitors are in the inductor current path, the charge energy Q_{C1} is drawn from the input source during this time interval. Since other parameters such as inductor size, diode resistance (r_d) and capacitances are constant, the $(1 - D)T$ interval lasts twice as long as the $d1T$ interval. Therefore, this relationship can be expressed by the number of current paths through the
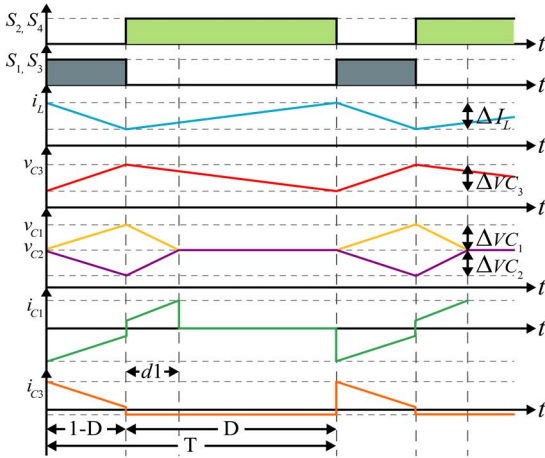
FIGURE 3. Converter's main waveforms with associated timing in CCM.

diodes in each mode of operation. This theory is accurate for the DVM with any number of stages.

$$m = \frac{d1_{path}}{(1-D)_{path}} = \frac{1}{2} \tag{12}$$

$$d1 = m(1-D)T = \frac{1(1-D)T}{2}, \tag{13}$$

where m is the ratio time of the *Mode* 1 to the *Mode* 3, $d1_{path}$ and $(1-D)_{path}$ are the number of inductor current paths through the diodes in $d1T$ and $(1-D)T$ time intervals, respectively. Substituting (12) into (7), The averaged state-space model of the converter obtained: (14)–(17), as shown at the bottom of the next page.

B. STEADY-STATE ANALYSIS
1) STEADY-STATE EQUATION AND VOLTAGE GAIN
The voltage gain for the converter can be obtained by using the volt-second balance on inductor voltage [16].

$$v_{C3} = \frac{2(v_{in} - i_L r_d)}{(1-D)}. \tag{18}$$

The i_L can be achieved by applying capacitor charge balance for capacitors current:

$$i_L = \frac{2v_{C3}}{R(1-D)}. \tag{19}$$

By substituting (19) in (18), the steady-state output voltage is equal to:

$$v_{out} = v_{C3} = \frac{2R(1-D)v_{in}}{R(1-D)^2 + 4r_d}. \tag{20}$$

Furthermore, the voltage gain for N number of capacitors can be obtained as:

$$\frac{v_{out}}{v_{in}} = (N+1)\frac{2R(1-D)}{2R(1-D)^2 + 8r_d}. \tag{21}$$

2) LOSSES AND EFFICIENCY
The existence of non-idealities in power elements leads to unavoidable losses and decreased efficiency. The converter losses are categorized into conduction losses and switching losses. This section represents the converter's non-ideal voltage gain and efficiency. The parasitic elements considered for conduction losses are the inductor's conduction (r_L), switches on-state resistance (r_{on}), and diodes forward voltage drop (v_f), as illustrated in Figure 4.

$$v_{out} = v_{C3} = \frac{(v_g - v_f)}{\left(\frac{1-D}{2}\right) + \frac{2(2r_{on}+r_L)}{R(1-D)}}, \tag{22}$$

$$i_{in} = i_L = \frac{2v_{out}}{R(1-D)}, \tag{23}$$

$$\eta = \frac{p_{out}}{p_{in}} = \frac{v_{out}i_{out}}{v_{in}i_{in}}. \tag{24}$$

C. COMPONENT SELECTION
By choosing proper values for inductors and capacitors, we can achieve a compact design with an acceptable ripple size and fulfill control demands such as zeros and poles movement on the RPH axis, improving the phase margin,

$$\begin{cases} \dot{X} = AX + BU \\ Y = MX + ZU \end{cases} \tag{6}$$

$$A = \begin{bmatrix} \frac{-r_d(1+D)}{2L} & \frac{d1}{L} - \frac{1-D}{2L} & \frac{d1}{L} - \frac{1-D}{2L} & -\frac{1-D}{2L} \\ \frac{1-2d1-D}{2C} & -\frac{1-D}{2Cr_d} & -\frac{1-D}{2Cr_d} & \frac{1-D}{2Cr_d} \\ \frac{-1+2d1+D}{2C} & -\frac{1-D}{2Cr_d} & \frac{1-D}{2Cr_d} & \frac{1-D}{2Cr_d} \\ \frac{1-D}{2C} & \frac{1-D}{2Cr_d} & \frac{1-D}{2Cr_d} & \frac{-1+D}{2Cr_d} - \frac{1}{RC} \end{bmatrix}, \tag{7}$$

$$B = \begin{bmatrix} \frac{1}{L} & 0 & 0 & 0 \end{bmatrix}^T, \tag{8}$$

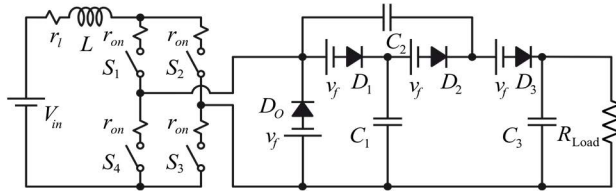$$M = \begin{bmatrix} 0 & 0 & 0 & 1 \end{bmatrix}, \tag{9}$$

$$Z = [0], \tag{10}$$

FIGURE 4. The CF-DVM with parasitic elements.

quality, and damping coefficient. The inductor current and capacitor voltage ripples in the ratio form are expressed as:

$$\varepsilon_{iL} = \frac{\Delta i_L}{2I_L}, \tag{25}$$

$$\varepsilon_{vC} = \frac{\Delta v_C}{2V_C}. \tag{26}$$

For this kind of converter, the ratio is designed to be $10 - 20\%$ for inductor current and $1 - 2\%$ for capacitor voltages [25].

1) CAPACITOR VOLTAGE AND INDUCTOR CURRENT RIPPLE
The inductor current and capacitor voltage ripples in CCM conditions according to (1), (2), and (5) are given by:

$$\Delta v_{C1} = \Delta v_{C2} = \frac{i_L (1 - D)}{2Cf} = \frac{v_{out}}{RCf}, \tag{27}$$

$$\Delta v_{C3} = \frac{v_{C3}D}{RCf}, \tag{28}$$

$$\Delta i_L = \frac{(v_{in} - v_{C1})(1 - D)}{Lf}. \tag{29}$$

2) CALCULATION OF SMALL-SIGNAL MODEL AND INPUT-TO-OUTPUT TRANSFER FUNCTION
Small-signal equations by using the small-perturbation technique are obtained as follows. The input variables and small-signal variables are given by (32) and (33), respectively. (30)–(33), as shown at the bottom of the next page.

TABLE 1. Converter parameters used for simulation and model verification.

Parameter	Symbol	Value
Output power	P_{out}	100W
Load	R_L	50Ω
Output voltage	V_{out}	70.5V
Input voltage	V_{in}	10V
Duty cycle	d	%75
Switching frequency	f_s	50kHz
Input inductor	L	1mH
Capacitance	C_1, C_2, C_3	10µF
MOSFET (FDP2614) ON resistance	r_{on}	25mΩ
Diodes forward voltage drop	v_f	0.24V
Diodes ON resistance	r_D	38mΩ

The input-to-output voltage (G_{vg}) and output voltage to duty cycle (G_{vd}) transfer functions are achieved based on the values used for simulations in Table 1.

$$G_{vg} = \frac{1.25e07s^2 + 1.042e13s}{s^4 + 1.252e06s^3 + 1.701e09s^2 + 1.346e12s + 55.39} \tag{34}$$

$$G_{vd} = \frac{-6.1633e05s\,(s + 8.333e05)\,(s - 18.78)}{s\,(s + 1.251e06)\,(s + 1313)\,(s + 20.49)}. \tag{35}$$

3) STABILITY CRITERIA FOR PASSIVE COMPONENTS
The pole-zero map of the G_{vd} transfer function in (35) is plotted in Figure 5. Accordingly, with the presence of a zero on the Right Half Plane (RHP), the converter is Non-Minimum Phase (NMP), and the closed-loop operation without a controller is unstable and has a non-regulated output, especially in high gain applications. Also, approaching the zero along the positive real axis toward the origin will increase control constraints, and the converter cannot achieve the desired fast response [2].

The NMP systems behave inversely to the input step changes because their open/close loop transfer functions can have the same zeros in the RHP. This means in case of an

$$\begin{cases} \dot{X} = AX + BU \\ Y = MX + ZU \end{cases}$$

$$A = \begin{bmatrix} \dfrac{-r_d\,(1 + D)}{2L} & 0 & 0 & -\dfrac{(1 - D)}{2L} \\ 0 & -\dfrac{(1 - D)}{2Cr_d} & -\dfrac{(1 - D)}{2Cr_d} & \dfrac{(1 - D)}{2Cr_d} \\ 0 & -\dfrac{(1 - D)}{2Cr_d} & -\dfrac{(1 - D)}{2Cr_d} & \dfrac{(1 - D)}{2Cr_d} \\ \dfrac{(1 - D)}{2C} & \dfrac{(1 - D)}{2Cr_d} & \dfrac{(1 - D)}{2Cr_d} & -\dfrac{(1 - D)}{2Cr_d} - \dfrac{1}{RC} \end{bmatrix}, \tag{14}$$

$$B = \begin{bmatrix} \frac{1}{L} & 0 & 0 & 0 \end{bmatrix}^T, \tag{15}$$

$$M = \begin{bmatrix} 0 & 0 & 0 & 1 \end{bmatrix}, \tag{16}$$

$$Z = [0]. \tag{17}$$
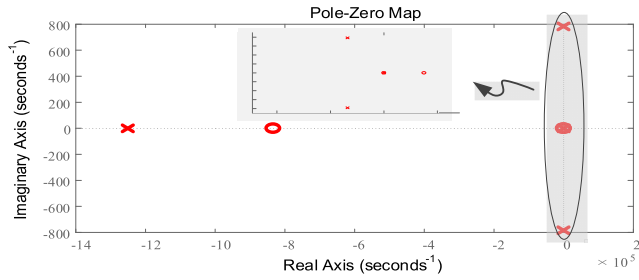
FIGURE 5. The pole-zero map of G_{vd} transfer function.

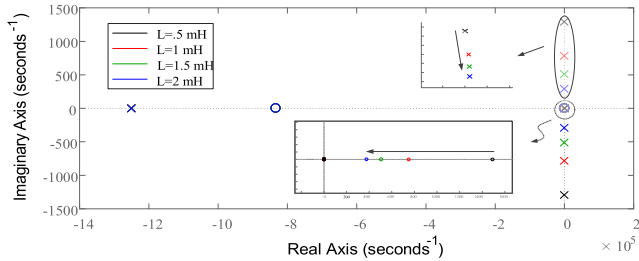**FIGURE 6.** Effect of inductance value on the pole-zero map.

FIGURE 7. Effect of capacitance value on the pole-zero map.

Conversely, as the capacitances increase, the conjugate poles move away from the real axis and then toward the origin. Nevertheless, the value of the capacitances does not affect the imaginary axis right side zero. Moreover, by reducing the value of the capacitances to achieve a better dynamic response, the converter's switching frequency must increase to maintain the desired voltage ripple, with respect to (27) and (28).

III. DESIGN OF THE FUZZY-BASED MPC OF CF-DVM
A. TS FUZZY REPRESENTATION OF CURRENT-FED DICKSON VOLTAGE MULTIPLIER
This subsection obtains the TSFM of the CF-DVM. The nonlinear dynamic model represented in (6) has some nonlinear terms. The sector nonlinearity approach can calculate the TSFM of this system. The nonlinear model is rephrased as follows:

$$\dot{x}(t) = \mathcal{A}x(t) + \mathcal{B}(x(t))u(t) + \mathcal{E}V_{in}$$
$$y(t) = \mathcal{C}x(t) \tag{36}$$

where $u(t)$ is the duty cycle and,

$$x(t) = [x_1(t), x_2(t), x_3(t), x_4(t)]^T$$
$$= [i_L(t), v_{c1}(t), v_{c2}(t), v_{c3}(t)]^T$$

increase in the input voltage, the output performs an undershoot before the response approaches its final value, which makes the controller design challenging.

As shown in Figure 6, the zero and the origin pole remain unchanged by increasing the inductance value (L). Also, the imaginary axis left side conjugate poles approach the real axis, which reduces the response oscillations. But on the other hand, approaching the RHP zero to the origin causes response oscillation. Thus, the RHP zero moves away from the origin with a lower inductance value and reduces the response oscillation. Nevertheless, according to (29), the converter's switching frequency must increase to maintain the inductor current ripple.

The effect of the capacitance value on zeros and poles is illustrated in Figure 7. Accordingly, the dominant conjugate poles approach the real axis as the capacitances decrease.
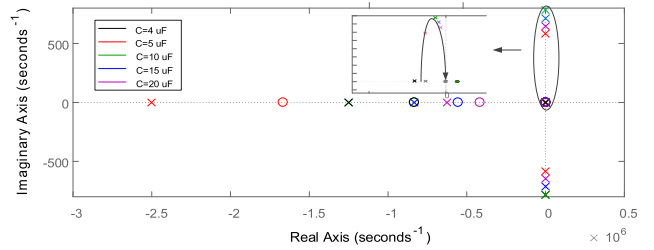
$$\dot{X} = AX + BU$$

$$A = \begin{bmatrix} \dfrac{-r_d(1+D)}{2L} & 0 & 0 & \dfrac{-D'}{2L} \\ 0 & \dfrac{-D'}{2Cr_d} & \dfrac{-D'}{2Cr_d} & \dfrac{D'}{2Cr_d} \\ 0 & \dfrac{-D'}{2Cr_d} & \dfrac{-D'}{2Cr_d} & \dfrac{D'}{2Cr_d} \\ \dfrac{D'}{2C} & \dfrac{D'}{2Cr_c} & \dfrac{D'}{2Cr_c} & \dfrac{-D'}{2Cr_c} - \dfrac{1}{RC} \end{bmatrix} \tag{30}$$

$$B = \begin{bmatrix} \dfrac{1}{L} & 0 & 0 & 0 \\ \dfrac{i_L r_d + v_{C3}}{2L} & \dfrac{-v_{C3}+v_{C2}+v_{C1}}{2Cr_d} & \dfrac{-v_{C3}+v_{C2}+v_{C1}}{2Cr_d} & \dfrac{-i_L}{2C} + \dfrac{v_{C3}-v_{C2}-v_{C1}}{2Cr_d} \end{bmatrix}^T, \tag{31}$$

$$\begin{bmatrix} \hat{v}_{in} & \hat{D} \end{bmatrix}^T \tag{32}$$

$$\begin{bmatrix} \hat{i}_L & \hat{v}_{C1} & \hat{v}_{C2} & \hat{v}_{C3} \end{bmatrix}^T. \tag{33}$$

$$\mathcal{A} = \begin{bmatrix} k_2 & 0 & 0 & k_4 \\ 0 & -k_6 & -k_6 & k_6 \\ 0 & -k_8 & -k_8 & k_8 \\ k_{10} & -k_{11} & -k_{11} & k_{11}+k_{13} \end{bmatrix}, \mathcal{E} = \begin{bmatrix} k_1 \\ 0 \\ 0 \\ 0 \end{bmatrix}$$

$$\mathcal{B}(x(t)) = \begin{bmatrix} k_3 x_1(t) + k_5 x_4(t) \\ k_7 x_4(t) - k_7(x_3(t)+x_2(t)) \\ k_9 x_4(t) - k_9(x_3(t)+x_2(t)) \\ -k_{10}x_1(t) - k_{12}(x_3(t)+x_2(t)) \\ +k_{12}x_4(t) \end{bmatrix},$$

$k_1 = \frac{1}{L}, k_2 = -\frac{r_D}{2L}, k_3 = k_2, k_4 = -\frac{1}{2}k_1, k_5 = \frac{1}{2}k_1,$
$k_6 = \frac{1}{2Cr_d}, k_7 = k_9 = k_{11} = -k_6, k_8 = k_{12} = k_6, k_{10} = \frac{1}{2C},$
and $k_{13} = -\frac{1}{RC}$.

According to the maximum and minimum values of each state based on the physical limitations, the premise variables are defined as follows:

$$z_1(t) = x_1(t),$$
$$z_2(t) = x_4(t),$$
$$z_3(t) = x_3(t) + x_2(t). \tag{37}$$

Moreover, the weighted average of each variable can be considered as follows:

$$z_1(t) = \bar{z}_1 M_1(t) + \underline{z}_1 M_2(t),$$
$$z_2(t) = \bar{z}_2 N_1(t) + \underline{z}_2 N_2(t),$$
$$z_3(t) = \bar{z}_3 Q_1(t) + \underline{z}_3 Q_2(t), \tag{38}$$

where $\bar{z}_i$ and $\underline{z}_i$ are the maximum and minimum values of the variables. Due to the orthogonality of the membership functions M_i, N_i and Q_i, each has:

$$M_1(t) = \frac{z_1(t) - \underline{z}_1}{\bar{z}_1 - \underline{z}_1}, M_2(t) = 1 - M_1(t),$$

$$N_1(t) = \frac{z_2(t) - \underline{z}_2}{\bar{z}_2 - \underline{z}_2}, N_2(t) = 1 - N_1(t),$$

$$Q_1(t) = \frac{z_3(t) - \underline{z}_3}{\bar{z}_3 - \underline{z}_3}, Q_2(t) = 1 - Q_1(t). \tag{39}$$

The state-space representation of each local linear subsystem of TSFM can be obtained as follows:

IF $z_1(t)$ is $M_j(t)$, $z_2(t)$ is $N_l(t)$ and $z_3(t)$ is $Q_p(t)$,

THEN $\dot{x}(t) = \mathcal{A}x(t) + \mathcal{B}_i u(t) + \mathcal{E}V_{in} \tag{40}$

where $i= 1, \ldots, 8$ and $l, j, p= 1, 2$ and

$$\mathcal{B}_1 = \begin{bmatrix} k_3\bar{z}_1 + k_5\bar{z}_2 \\ k_7\bar{z}_2 - k_7\bar{z}_3 \\ k_9\bar{z}_2 - k_9\bar{z}_3 \\ -k_{10}\bar{z}_1 - k_{12}\bar{z}_3 + k_{12}\bar{z}_2 \end{bmatrix},$$

$$\mathcal{B}_2 = \begin{bmatrix} k_3\bar{z}_1 + k_5\bar{z}_2 \\ k_7\bar{z}_2 - k_7\underline{z}_3 \\ k_9\bar{z}_2 - k_9\underline{z}_3 \\ -k_{10}\bar{z}_1 - k_{12}\underline{z}_3 + k_{12}\bar{z}_2 \end{bmatrix},$$

$$\mathcal{B}_3 = \begin{bmatrix} k_3\bar{z}_1 + k_5\underline{z}_2 \\ k_7\underline{z}_2 - k_7\bar{z}_3 \\ k_9\underline{z}_2 - k_9\bar{z}_3 \\ -k_{10}\bar{z}_1 - k_{12}\bar{z}_3 + k_{12}\underline{z}_2 \end{bmatrix},$$

$$\mathcal{B}_4 = \begin{bmatrix} k_3\bar{z}_1 + k_5\underline{z}_2 \\ k_7\underline{z}_2 - k_7\underline{z}_3 \\ k_9\underline{z}_2 - k_9\underline{z}_3 \\ -k_{10}\bar{z}_1 - k_{12}\underline{z}_3 + k_{12}\underline{z}_2 \end{bmatrix},$$

$$\mathcal{B}_5 = \begin{bmatrix} k_3\underline{z}_1 + k_5\bar{z}_2 \\ k_7\bar{z}_2 - k_7\bar{z}_3 \\ k_9\bar{z}_2 - k_9\bar{z}_3 \\ -k_{10}\underline{z}_1 - k_{12}\bar{z}_3 + k_{12}\bar{z}_2 \end{bmatrix},$$

$$\mathcal{B}_6 = \begin{bmatrix} k_3\underline{z}_1 + k_5\bar{z}_2 \\ k_7\bar{z}_2 - k_7\underline{z}_3 \\ k_9\bar{z}_2 - k_9\underline{z}_3 \\ -k_{10}\underline{z}_1 - k_{12}\underline{z}_3 + k_{12}\bar{z}_2 \end{bmatrix},$$

$$\mathcal{B}_7 = \begin{bmatrix} k_3\underline{z}_1 + k_5\underline{z}_2 \\ k_7\underline{z}_2 - k_7\bar{z}_3 \\ k_9\underline{z}_2 - k_9\bar{z}_3 \\ -k_{10}\underline{z}_1 - k_{12}\bar{z}_3 + k_{12}\underline{z}_2 \end{bmatrix},$$

$$\mathcal{B}_8 = \begin{bmatrix} k_3\underline{z}_1 + k_5\underline{z}_2 \\ k_7\underline{z}_2 - k_7\underline{z}_3 \\ k_9\underline{z}_2 - k_9\underline{z}_3 \\ -k_{10}\underline{z}_1 - k_{12}\underline{z}_3 + k_{12}\underline{z}_2 \end{bmatrix}.$$

Finally, the overall fuzzy model of the CF-DVM is obtained by fuzzy blending in the following:

$$\dot{x}(t) = \sum_{i=1}^{8} h_i(t) (\mathcal{A}x(t) + \mathcal{B}_i u(t) + \mathcal{E}V_{in})$$
$$y(t) = \mathcal{C}x(t) \tag{41}$$

where

$$h_1(t) = M_1(t) N_1(t) Q_1(t),$$
$$h_2(t) = M_1(t) N_1(t) Q_2(t),$$
$$h_3(t) = M_1(t) N_2(t) Q_1(t),$$
$$h_4(t) = M_1(t) N_2(t) Q_2(t),$$
$$h_5(t) = M_2(t) N_1(t) Q_1(t),$$
$$h_6(t) = M_2(t) N_1(t) Q_2(t),$$
$$h_7(t) = M_2(t) N_2(t) Q_1(t),$$
$$h_8(t) = M_2(t) N_2(t) Q_2(t). \tag{42}$$

Based on the derived model, the fuzzy-based MPC of the CF-DVM is designed in the following subsection.

B. TSFM-BASED MODEL PREDICTIVE CONTROL OF CF-DVM

MPC requires a dynamical model of the controlled system to predict the system states' future behavior. The main advantages of the MPC are optimal performance and guaranteed constrained performance of the system [37]. In order to design the TSFM-based MPC for the CF-DVM, the obtained TSFM in (41) is employed. Then, the optimization problem is converted to a QP optimization that is solved in each time step. The suitable value of the control signal is obtained based on the minimization of the QP optimization. The fuzzy MPC scheme based on the discrete-time model of the TSFM is

defined as follows:

$$J(t) = \tilde{x}^T(N|t)\,\mathfrak{D}\tilde{x}(N|t)$$
$$+ \sum_{k=0}^{N-1} \tilde{x}^T(k|t)\,Q\tilde{x}(k|t) + \tilde{u}^T(k|t)\,\mathfrak{R}\tilde{u}(k|t)$$

Subject to:

$$x(k+1|t) = \mathcal{A}x(k|t) + B_h u(k|t) + \mathcal{E}V_{in}$$
$$y(t) = \mathcal{C}x(t)$$
$$u(k|t) \in \mathcal{U}$$
$$x(k|t) \in \mathcal{X} \tag{43}$$

where $B_h = \sum_{i=1}^{8} h_i(t)\,\mathcal{B}_i$, $\tilde{x}(t) = y(t) - x_e(t)$, $\tilde{u}(t) = u(t) - u_e(t)$, x_e and u_e are the desired values of the system states and control input. Also, N is the prediction horizon, $\mathfrak{D} > 0$, $Q > 0$, and $\mathfrak{R} > 0$ are proper weighting coefficient matrices. The sets $\mathcal{X}$ and $\mathcal{U}$ are the polyhedrons that specify the constraints on the system states and the control input, respectively.

To implement the fuzzy-based MPC, the vector form of the optimization problem (43) must be obtained. Therefore, considering the predetermined prediction horizon N, the system's output can be calculated as follows:

$$\mathcal{Y} = \mathcal{M}x(k|t) + \mathcal{N}U + \mathcal{G}V_{in}, \tag{44}$$

where

$$\mathcal{Y} = \begin{bmatrix} y(k+1|t) \\ y(k+2|t) \\ \vdots \\ y(k+N|t) \end{bmatrix}, \quad \mathcal{M} = \begin{bmatrix} \mathcal{CA} \\ \mathcal{CA}^2 \\ \vdots \\ \mathcal{CA}^N \end{bmatrix},$$

$$\mathcal{U} = \begin{bmatrix} u(k|t) \\ u(k+1|t) \\ \vdots \\ u(k+N-1|t) \end{bmatrix},$$

$$\mathcal{N} = \begin{bmatrix} \mathcal{CB}_h & 0 & \cdots & 0 \\ \mathcal{CAB}_h & \mathcal{CB}_h & \cdots & 0 \\ \vdots & \vdots & \vdots & \vdots \\ \mathcal{CA}^{N-1}B_h & \mathcal{CA}^{N-2}B_h & \cdots & \mathcal{CB}_h \end{bmatrix},$$

$$\mathcal{V}_{in} = \begin{bmatrix} V_{in}(k|t) \\ V_{in}(k+1|t) \\ \vdots \\ V_{in}(k+N-1|t) \end{bmatrix}, \quad.$$

$$\mathcal{G} = \begin{bmatrix} \mathcal{CE} & 0 & \cdots & 0 \\ \mathcal{CAE} & \mathcal{CE} & \cdots & 0 \\ \vdots & \vdots & \vdots & \vdots \\ \mathcal{CA}^{N-1}\mathcal{E} & \mathcal{CA}^{N-2}\mathcal{E} & \cdots & \mathcal{CE} \end{bmatrix}.$$

So, the vector form of the cost function can be obtained as:

$$J(N) = 2\mathcal{F}\mathcal{U} + U^T\mathcal{H}U + k, \tag{45}$$

where $\mathcal{F} = (\mathcal{M}x(k|t) + \mathcal{G}V_{in} - b)\,Q\mathcal{N}$, $\mathcal{H} = \mathcal{N}^T Q\mathcal{N} + \mathfrak{R}$, $\mathcal{R} = diag(\mathfrak{R},\ldots,\mathfrak{R})$, $\mathcal{Q} = diag(\mathcal{Q},\ldots,\mathcal{Q},\mathfrak{D})$, $b =$
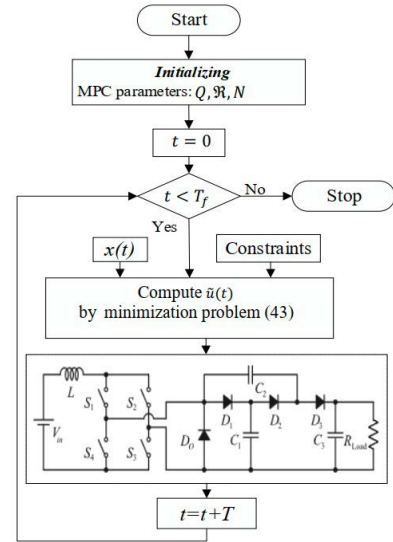

FIGURE 8. Total flowchart of the proposed control method. *T* and *T_f* are the sampling time and the final time.
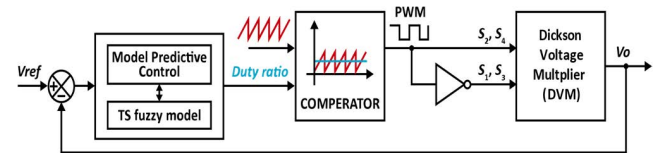

FIGURE 9. Block diagram of the converter's control system.

$\left[x_e^T(k+1|t), x_e^T(k+2|t),\ldots, x_e^T(k+N|t)\right]^T$, and $k = (\mathcal{M}x(k|t) + \mathcal{G}V_{in} - b)\,\mathcal{Q}(\mathcal{M}x(k|t) + \mathcal{G}V_{in} - \mathcal{E})$.

According to (45), k does not affect the optimization problem. Consequently, the cost function is similar to a QP optimization problem and has less computational complexity than the online optimization problem based on the linear matrix inequality [38]. Moreover, the design process of the proposed control method is shown in Figure 8. The block diagram of the control system is illustrated in Figure 9.

IV. SIMULATION RESULTS
This section presents simulations and experimental results to evaluate the proposed modeling and control methods. The converter with the parameters shown in Table 1 is simulated to validate the proposed model.

A. OPEN-LOOP OPERATION
First, to demonstrate the accuracy of the proposed modeling approach, the transients of the output voltage ($v_{c3}(t)$) and input inductor current ($i_L(t)$) are plotted in Figure 10 and Figure 11, respectively. Accordingly, the obtained results confirm consistency and accuracy between modeling and simulation responses of the CF-DVM.

Moreover, to demonstrate the feasibility of the theoretical concepts, a laboratory prototype of the proposed converter was implemented and tested. The experimental test setup is shown in Figure 12. The converter's output voltage and input current transients are shown in Figure 13, which shows
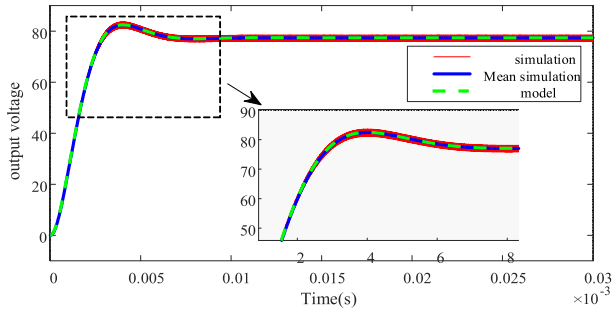
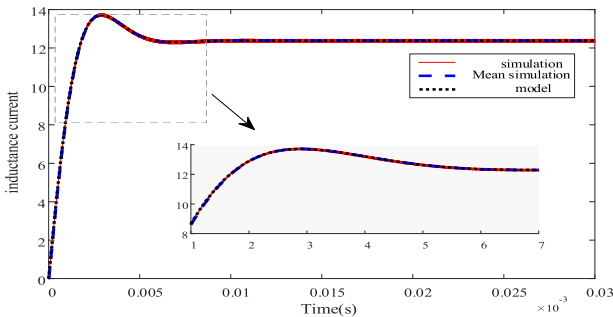**FIGURE 10.** Comparison between the CF-DVM's output voltage for the proposed model and simulation.

FIGURE 11. Comparison between inductor's current of the proposed model and simulation.
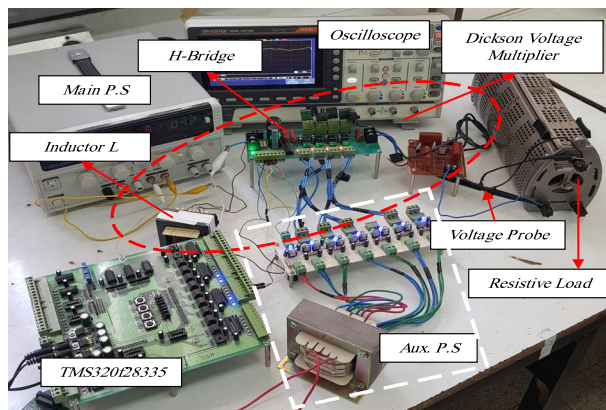

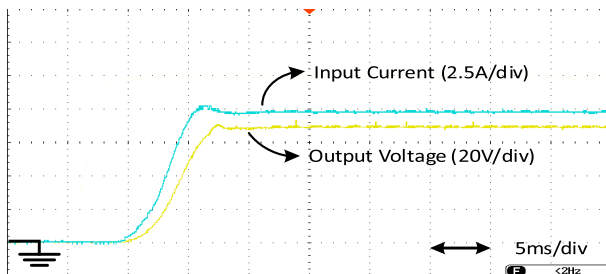**FIGURE 12.** The experimental laboratory setup.

FIGURE 13. Experimental results of the converter's output voltage and inductor current waveforms.

consistency with simulations. The converter's output voltage measured to be $V_{out} = 70.5V$ and the input current at $I_{in} = 10.7A$ that validate the calculated values in (22) and (23), respectively. The output power of the converter with the input voltage of $V_{in} = 10V$, was measured to be $P_{out} = 100W$. Figure 14 shows the output voltage ripple of the capacitors alongside the switches S_2 and S_4 gating pulse.
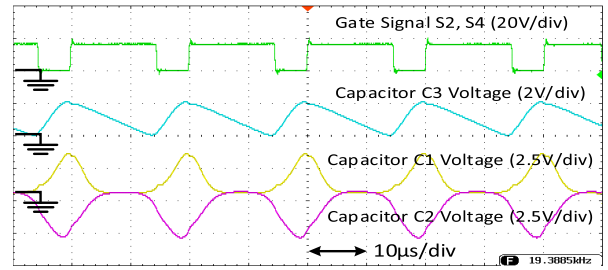

FIGURE 14. Experimental results of the capacitors voltage ripple with switches S_2 and S_4 gating pulse waveforms.
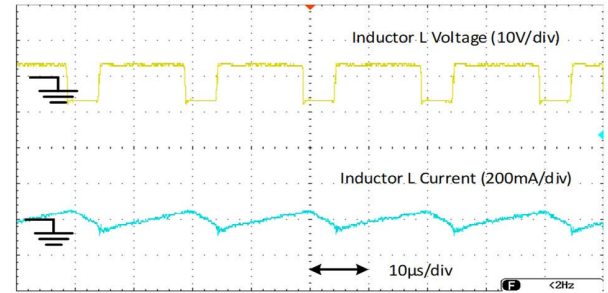

FIGURE 15. Experimental results of the inductor's voltage and current ripple waveforms.
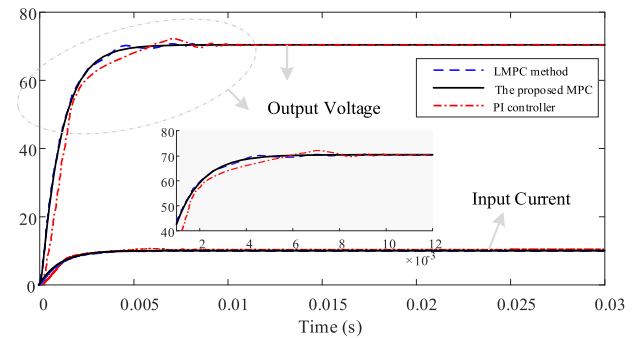

FIGURE 16. Comparison between the CF-DVM's output voltage for the proposed MPC, the LMPC, and the PI-controller.

Figure 15 demonstrates the inductor voltage and current ripple. Finally, the obtained waveforms from the experimental results confirm the accuracy of the modeling and simulation under open-loop operation. It should be noted that the minor differences between the theoretical and experimental results are due to the influence of parasitic elements.

B. CLOSED-LOOP OPERATION

In this scenario, the output voltage of the CF-DVM is controlled by the TSFM-based MPC. To demonstrate the merits of the proposed MPC, simulations are used to compare the converter's output voltage with the proposed MPC, the LMPC [33], and the PI-controller. As shown in Figure 16, the proposed MPC's performance is more precise and faster than the PI-controller and the LMPC. Moreover, the LMPC's output voltage tracking error is higher due to the linearization of the nonlinear model in the design process. Meanwhile, the TSFM of the CF-DVM represents the exact model of the nonlinear systems. Therefore, the predicted output is more accurate and improves the controller's performance.
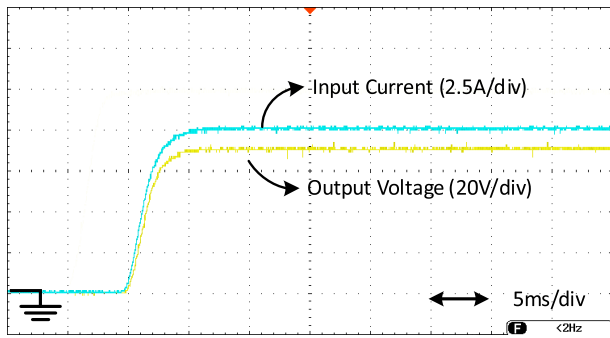
FIGURE 17. Experimental results of the converter's output voltage and inductor current waveforms.
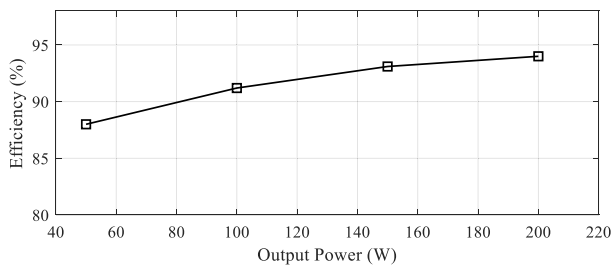

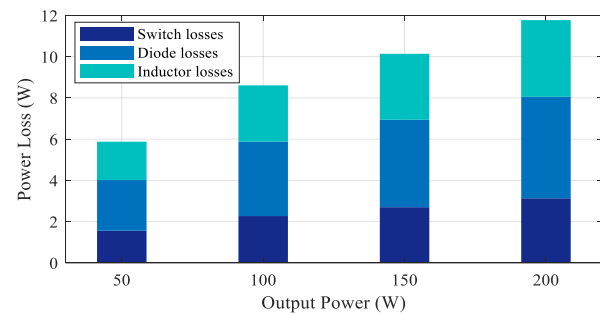**FIGURE 18.** The efficiency of the CF-DVM.

FIGURE 19. The power losses of the CF-DVM.

Moreover, the laboratory prototype was tested under closed-loop operation to illustrate the advantages of theoretical concepts and the proposed control method. The converter's output voltage and input current under the TSFM-based MPC are shown in Figure 17. Accordingly, the performance of the proposed MPC in the experimental test is promising. In addition, the obtained waveforms from the experimental results confirm the accuracy of the modeling and controller design under closed-loop operation. It should be noted that the minor differences between the theoretical and experimental results are due to the influence of parasitic elements. Finally, the efficiency and power losses diagrams are shown in Figures 18, 19, respectively.

V. CONCLUSION
This paper presented a new dynamic model and control approach of the CF-DVM. The effect of different passive component values (inductor and capacitors) on the converter's dynamic response was studied. Furthermore, the converter's state-space model and transfer functions were derived to accurately calculate the converter's transient and steady-state behaviors. Also, by considering the switching interval

of d_1 the dynamic equations can be easily obtained for an arbitrary n-stage CF-DVM. Moreover, the effect of parasitic elements on the converter's performance and efficiency in the steady-state operation were studied. Afterward, the TSFM of the CF-DVM was presented based on the sector nonlinearity approach. Then, a highly accurate and responsive fuzzy-based MPC was designed (thanks to the precise proposed dynamic model) to control the CF-DVM's output voltage. Then, an exact TS fuzzy model of the calculated nonlinear model is computed. Finally, the derived dynamic model and control method was validated through simulations and experimental results with a laboratory prototype of the CF-DVM. The results demonstrate the promising advantages of the presented methods.

REFERENCES
[1] B. P. Baddipadiga and M. Ferdowsi, "A high-voltage-gain DC–DC converter based on modified Dickson charge pump voltage multiplier," *IEEE Trans. Power Electron.*, vol. 32, no. 10, pp. 7707–7715, Oct. 2016.
[2] M. Forouzesh, P. Y. Siwakoti, A. S. Gorji, F. Blaabjerg, and B. Lehman, "Step-up DC–DC Converters: A comprehensive review of voltage-boosting techniques, topologies, and applications," *IEEE Trans. Power Electron.*, vol. 32, no. 12, pp. 9143–9178, Dec. 2017.
[3] T.-D. Duong, M.-K. Nguyen, T.-T. Tran, Y.-C. Lim, and J.-H. Choi, "Transformerless high step-up DC–DC converters with switched-capacitor network," *Electronics*, vol. 8, no. 12, p. 1420, Nov. 2019.
[4] B. Axelrod, Y. Berkovich, and A. Ioinovici, "Switched-capacitor/switched-inductor structures for getting transformerless hybrid DC–DC PWM converters," in *Proc. IEEE Int. Symp. Circuits Syst. (ISCAS)*, vol. 55, no. 2, Mar. 2008, pp. 687–696.
[5] D. Marroqui, A. Garrigós, C. Torres, C. Orts, J. M. Blanes, and R. Gutierrez, "Interleaved, switched inductor and high-gain wide bandgap based boost converter proposal," *Energies*, vol. 14, no. 4, p. 800, Feb. 2021.
[6] M. Rezaie and V. Abbasi, "Ultrahigh step-up DC–DC converter composed of two stages boost converter, coupled inductor, and multiplier cell," *IEEE Trans. Ind. Electron.*, vol. 69, no. 6, pp. 5867–5878, Jun. 2021.
[7] M. S. Bhaskar, N. Gupta, S. Selvam, D. J. Almakhles, P. Sanjeevikumar, J. S. M. Ali, and S. Umashankar, "A new hybrid zeta-boost converter with active quad switched inductor for high voltage gain," *IEEE Access*, vol. 9, pp. 20022–20034, 2021.
[8] R. Kumari, M. Pandit, and K. S. Sherpa, "A comprehensive study on evolution and advancement of DC–DC cascaded converters: A review," *Aust. J. Electr. Electron. Eng.*, vol. 19, pp. 1–16, Jan. 2021.
[9] A. Alzahrani, P. Shamsi, and M. Ferdowsi, *Analysis and Design of Bipolar Dickson DC–DC Converter*. Champaign, IL, USA: IEEE, 2017.
[10] A. Rajaei, R. Khazan, M. Mahmoudian, M. Mardaneh, and M. Gitizadeh, "A dual inductor high step-up DC/DC converter based on the Cockcroft–Walton multiplier," *IEEE Trans. Power Electron.*, vol. 33, no. 11, pp. 9699–9709, Nov. 2018.
[11] T. Das, S. Prasad, S. Dam, and P. Mandal, "A pseudo cross-coupled switch-capacitor based DC–DC boost converter for high efficiency and high power density," *IEEE Trans. Power Electron.*, vol. 29, no. 11, pp. 5961–5974, Nov. 2014.
[12] S. Sanders, E. Alon, H.-P. Le, M. Seeman, M. John, and V. Ng, "The road to fully integrated DC–DC conversion via the switched-capacitor approach," *IEEE Trans. Power Electron.*, vol. 28, no. 9, pp. 4146–4155, Sep. 2012.
[13] A. Stillwell and R. C. N. Pilawa-Podgurski, "A resonant switched-capacitor converter with GaN transistors for series-stacked processors with 99.8% power delivery efficiency," in *Proc. IEEE Energy Convers. Congr. Expo. (ECCE)*, Sep. 2015, pp. 563–570.
[14] A. C. Baughman and M. Ferdowsi, "Double-tiered switched-capacitor battery charge equalization technique," *IEEE Trans. Ind. Electron.*, vol. 55, no. 6, pp. 2277–2285, Jun. 2008.
[15] A. Ajami, H. Ardi, and A. Farakhor, "A novel high step-up DC/DC converter based on integrating coupled inductor and switched-capacitor techniques for renewable energy applications," *IEEE Trans. Power Electron.*, vol. 30, no. 8, pp. 4255–4263, Aug. 2014.

[16] Y. Berkovich, B. Axelrod, D. Shoshani, and Y. Beck, "DC–DC converter based on the bipolar boost converter and Dickson voltage multiplier," in *Proc. IEEE Int. Energy Conf. (ENERGYCON)*, Jun. 2018, pp. 1–6.

[17] A. Mahmoud, M. Alhawari, B. Mohammad, H. Saleh, and M. Ismail, "A multi-input, multi-output power management unit using Dickson charge pump for energy harvesting applications," in *Proc. IEEE 59th Int. Midwest Symp. Circuits Syst. (MWSCAS)*, Oct. 2016, pp. 1–4.

[18] D. Vinko, "Applicability of Dickson charge pump in energy harvesting systems: Experimental validation of energy harvesting charge pump model," *Radioengineering*, vol. 27, no. 2, p. 511, 2018.

[19] A. Cabrini, L. Gobbi, and G. Torelli, "Voltage gain analysis of integrated fibonacci-like charge pumps for low power applications," *IEEE Trans. Circuits Syst. II, Exp. Briefs*, vol. 54, no. 11, pp. 929–933, Nov. 2007.

[20] W. Do and K. Eguchi, "Analysis of parallel connected Fibonacci switched capacitor converter," *Energy Rep.*, vol. 6, pp. 362–367, Feb. 2020.

[21] J. C. Rosas-Caro, J. C. Mayo-Maldonado, F. Mancilla-David, A. Valderrabano-Gonzalez, and F. B. Carbajal, "Single-inductor resonant switched capacitor voltage multiplier with safe commutation," *IET Power Electron.*, vol. 8, no. 4, pp. 507–516, Apr. 2015.

[22] H. Wu, T. Mu, H. Ge, and Y. Xing, "Full-range soft-switching-isolated buck-boost converters with integrated interleaved boost converter and phase-shifted control," *IEEE Trans. Power Electron.*, vol. 31, no. 2, pp. 987–999, Feb. 2015.

[23] F. H. Dupont, C. Rech, R. Gules, and J. R. Pinheiro, "Reduced-order model and control approach for the boost converter with a voltage multiplier cell," *IEEE Trans. Power Electron.*, vol. 28, no. 7, pp. 3395–3404, Jul. 2012.

[24] P. V. Das, P. Karuppanan, A. K. Singh, and B. Chitti Babu, "Modelling, simulation and analysis of high step up DC–DC converter using coupled inductor and voltage multiplier cell using PSCAD," *Int. J. Model. Simul.*, vol. 40, no. 1, pp. 29–36, Jan. 2020.

[25] J. Leyva-Ramos, R. Mota-Varona, M. G. Ortiz-Lopez, L. H. Diaz-Saldierna, and D. Langarica-Cordoba, "Control strategy of a quadratic boost converter with voltage multiplier cell for high-voltage gain," *IEEE J. Emerg. Sel. Topics Power Electron.*, vol. 5, no. 4, pp. 1761–1770, Dec. 2017.

[26] M. Appikonda and D. Kaliaperumal, "Modelling and control of dual input boost converter with voltage multiplier cell," *IET Circuits, Devices Syst.*, vol. 13, no. 8, pp. 1267–1276, Nov. 2019.

[27] P. Mangaiyarkarasi and A. Kavitha, "Dynamics and control of voltage multiplier cells integrated boost converter," *IET Circuits, Devices Syst.*, vol. 11, no. 1, pp. 68–79, Jan. 2017.

[28] B. Zhu, Q. Zeng, M. Vilathgamuwa, Y. Li, and Y. Chen, "A generic control-oriented model order reduction approach for high step-up DC/DC converters based on voltage multiplier," *Energies*, vol. 12, no. 10, p. 1971, May 2019.

[29] S. Bououden, M. Chadli, and I. Zelinka, "LMI approach of constrained fuzzy model predictive control of DC–DC boost converter," in *Prediction, Modeling and Analysis of Complex Systems*. Cham, Switzerland: Springer, 2014, pp. 205–217.

[30] T. Geyer, G. Papafotiou, and M. Morari, "Hybrid model predictive control of the step-down DC–DC converter," *IEEE Trans. Control Syst. Technol.*, vol. 16, no. 6, pp. 1112–1124, Nov. 2008.

[31] O. Abdel-Rahim and H. Wang, "A new high gain DC–DC converter with model-predictive-control based MPPT technique for photovoltaic systems," *CPSS Trans. Power Electron. Appl.*, vol. 5, no. 2, pp. 191–200, Jun. 2020.

[32] E. F. Camacho and C. B. Alba, *Model Predictive Control*. New York, NY, USA: Springer, 2013.

[33] L. Cheng, P. Acuna, R. P. Aguilera, J. Jiang, S. Wei, J. E. Fletcher, and D. D. C. Lu, "Model predictive control for DC–DC boost converters with reduced-prediction horizon and constant switching frequency," *IEEE Trans. Power Electron.*, vol. 33, no. 10, pp. 9064–9075, Oct. 2017.

[34] B. Axelrod and Y. Berkovich, "DC–DC converter based on the switched-coupled-inductor quadratic boost converter and diode-capacitor Dickson multiplier," in *Proc. 19th Eur. Conf. Power Electron. Appl. (EPE ECCE Europe)*, Sep. 2017, p. 1.

[35] M. Farbood, M. Sha-Sadeghi, A. Izadian, and T. Niknam, "Advanced model predictive MPPT and frequency regulation in interconnected wind turbine drivetrains," in *Proc. IEEE Energy Convers. Congr. Expo. (ECCE)*, Sep. 2018, pp. 3658–3663, doi: 10.1109/ECCE.2018.8557950.

[36] D. Shen, C.-C. Lim, and P. Shi, "Robust fuzzy model predictive control for energy management systems in fuel cell vehicles," *Control Eng. Pract.*, vol. 98, May 2020, Art. no. 104364.

[37] M. Farbood, M. Shasadeghi, T. Niknam, and B. Safarinejadian, "Fuzzy Lyapunov-based model predictive sliding-mode control of nonlinear systems: An ellipsoid recursive feasibility approach," *IEEE Trans. Fuzzy Syst.*, vol. 30, no. 6, pp. 1929–1938, Jun. 2021.

[38] K. Tanaka and H. O. Wang, *Fuzzy Control Systems Design and Analysis: A Linear Matrix Inequality Approach*. Hoboken, NJ, USA: Wiley, 2004.

YOUSEF NIAZI was born in 1993. He received the B.Sc. and M.Sc. degrees in electrical engineering from Ilam University, Ilam, Iran, in 2015 and 2017, respectively. He is currently pursuing the Ph.D. degree in power electronics research domain with the Shiraz University of Technology, Shiraz, Iran. His research interests include design, modeling, simulation and fabrication of power electronics converters, voltage multiplier circuits, and renewable energy.

AMIRHOSSEIN RAJAEI (Member, IEEE) was born in Jahrom, Iran. He received the B.Sc. degree in electrical engineering from Shiraz University, Shiraz, Iran, in 2006, and the M.Sc. and Ph.D. degrees in electrical engineering from Tarbiat Modares University, Tehran, Iran, in 2009 and 2013, respectively. He is currently an Associate Professor with the Shiraz University of Technology, Shiraz. He is also a Frequent Reviewer of IEEE TRANSACTIONS ON POWER ELECTRONICS, IEEE TRANSACTIONS ON INDUSTRIAL ELECTRONICS, and IEEE JOURNAL OF EMERGING AND SELECTED TOPICS IN POWER ELECTRONICS. His research interests include power converters, modeling and design, and their applications in microgrids.

MOHSEN FARBOOD received the B.Sc. degree from Shahid Bahonar Technical and Engineering College, Shiraz, Iran, in 2015, and the M.Sc. degree from the Shiraz University of Technology, Shiraz, Iran, in 2017, where he is currently pursuing the Ph.D. degree in control engineering. His research interests include fuzzy-based nonlinear control, predictive control, and control of power systems.

VAHID MORADZADEH TEHRANI was born in Shiraz, Iran, in September 1997. He received the B.Sc. degree in electrical engineering from the Firouzabad Institute of Higher Education, Firuzabad, Iran, in 2019. He is currently pursuing the M.Sc. degree in electrical engineering with the Shiraz University of Technology, Shiraz. His research interests include modeling and designing DC/DC converters, DC/AC inverters, renewable energy power conversion, and motor drive systems.

MOKHTAR SHASADEGHI is currently an Associate Professor with the Shiraz University of Technology, Shiraz, Iran. His research interests include fuzzy control, linear matrix inequalities, and optimization.

MAHDI SHAHPARASTI (Senior Member, IEEE) received the M.Sc. and Ph.D. degrees (Hons.) in electrical engineering from Tarbiat Modares University, Tehran, Iran, in 2010 and 2014, respectively. For more than seven years, from 2010 to 2014 and 2016 to 2017, he was an Research and Development Engineer with JDEVS Company, Tehran, in designing power converters for UPS, motor drive and hybrid energy systems. In 2015, he was a Postdoctoral Researcher with the Technical University of Catalonia, Barcelona, Spain, where he was involved in a project with Ingeteam Company for controlling high-power grid-connected converters. In 2016, he worked as an Assistant Professor with the Department of Electrical Engineering, East Tehran Branch of Azad University, Tehran. From 2017 to 2019, he was awarded a two- year Marie Skłodowska-Curie Fellowship to develop interlinking converters for power-to-gas plants. Then, he joined the University of Southern Denmark as a Postdoctoral Researcher involved in developing the hardware and control of DC/DC and DC/AC converters, from 2019 to 2021. He is currently an Assistant Professor in power electronics with the University of Vaasa, Finland. His research interests include hardware design, control, stability and dynamic analysis of power electronic systems, power quality, microgrids, renewable energy resources, and motor drive systems.

• • •